

ENDOR and ESEEM investigation of the Ni-containing superoxide dismutase

Hong-In Lee · Jin-Won Lee · Tran-Chin Yang ·
Sa-Ouk Kang · Brian M. Hoffman

Received: 16 June 2009 / Accepted: 14 August 2009 / Published online: 26 August 2009
© SBIC 2009

Abstract Superoxide dismutases (SODs) protect cells against oxidative stress by disproportionating O_2^- to H_2O_2 and O_2 . The recent finding of a nickel-containing SOD (Ni-SOD) has widened the diversity of SODs in terms of metal contents and SOD catalytic mechanisms. The coordination and geometrical structure of the metal site and the related electronic structure are the keys to understanding the dismutase mechanism of the enzyme. We performed Q-band ^{14}N , $^{1/2}H$ continuous wave (CW) and pulsed electron–nuclear double resonance (ENDOR) and X-band ^{14}N electron spin echo envelope modulation (ESEEM) on the resting-state Ni-SOD extracted from *Streptomyces seoulensis*. In-depth analysis of the data obtained from the

multifrequency advanced electron paramagnetic resonance techniques detailed the electronic structure of the active site of Ni-SOD. The analysis of the field-dependent Q-band ^{14}N CW ENDOR yielded the nuclear hyperfine and quadrupole coupling tensors of the axial N_δ of the His-1 imidazole ligand. The tensors are coaxial with the g -tensor frame, implying the g -tensor direction is modulated by the imidazole plane. X-band ^{14}N ESEEM characterized the hyperfine coupling of N_ϵ of His-1 imidazole. The nuclear quadrupole coupling constant of the nitrogen suggests that the hydrogen-bonding between $N_\epsilon-H$ and O_{Glu-17} present for the reduced-state Ni-SOD is weakened or broken upon oxidizing the enzyme. Q-band 1H CW ENDOR and pulsed 2H Mims ENDOR showed a strong hyperfine coupling to the proton(s) of the equatorially coordinated His-1 amine and a weak hyperfine coupling to either the proton(s) of a water in the pocket at the side opposite the axial N_δ or the proton of a water hydrogen-bonded to the equatorial thio-late ligand.

H.-I. Lee (✉)
Department of Chemistry,
Kyungpook National University,
Daegu 702-701, Republic of Korea
e-mail: leehi@knu.ac.kr

J.-W. Lee
Department of Life Science,
Research Center for Natural Sciences,
Hanyang University,
Seoul 133-791, Republic of Korea

S.-O. Kang (✉)
Laboratory of Biophysics,
School of Biological Sciences,
Institute of Microbiology,
Seoul National University,
Seoul 151-742, Republic of Korea
e-mail: kangsaou@snu.ac.kr

T.-C. Yang · B. M. Hoffman (✉)
Department of Chemistry,
Northwestern University,
Evanston, IL 60208-3113, USA
e-mail: bmh@northwestern.edu

Keywords Nickel-containing superoxide dismutase ·
Electron paramagnetic resonance ·
Electron-nuclear double resonance ·
Electron spin echo envelope modulation

Abbreviations

CuZn-SOD Copper- and zinc-containing superoxide dismutase
CW Continuous wave
ENDOR Electron–nuclear double resonance
EPR Electron paramagnetic resonance
ESEEM Electron spin echo envelope modulation
Ni-SOD Nickel-containing superoxide dismutase
SOD Superoxide dismutase

Introduction

Superoxide dismutases (SODs) catalyze disproportionation of superoxide (O_2^-) to hydrogen peroxide (H_2O_2) and molecular oxygen (O_2) to protect cells against oxidative stress [1–4]. SODs are found in all living organisms and all have redox-active transition metals in their active sites. The most well known one, found in both eukaryotes and prokaryotes, contains copper and zinc (CuZn-SOD). Other SODs contain manganese or iron. Crystallographic studies of the SODs revealed histidine-rich metal centers. In CuZn-SOD, copper and zinc are bridged by the imidazolate of a histidine residue, whereas manganese-containing SOD and iron-containing SOD have mononuclear transition metal centers. In the resting state of CuZn-SOD, the Cu(II) site is pentacoordinated with four histidine residues, including the bridging histidine, and one solvent-accessible ligand site. The Zn(II) site has three histidine ligands, including the bridging histidine, and one oxygen ligand of the carboxylate group of an aspartate residue [5–8]. The metal centers of both the oxidized manganese-containing SOD and the oxidized iron-containing share identical trigonal bipyramidal geometries. In those, two nitrogen atoms of histidine side chains and one oxygen atom of aspartate occupy the three equatorial ligand positions of the bipyramidal coordination, and a solvent molecule and one histidine imidazole occupy the remaining two axial positions [9–14].

The diversity of SODs in terms of metal contents has become even wider. Recent isolation of SODs from *Streptomyces* species revealed a nickel-containing SOD (Ni-SOD) [15, 16]. The amino acid sequence analysis of the enzyme exhibited no sequence homology to any known SODs [17]. The finding of Ni-SOD is also of interest because copper, iron, and manganese ions can catalyze disproportionation of superoxide anions in aqueous solution but nickel ion does not, indicating that Ni-SOD is a new class among the SODs. The 3D coordination environments and the electronic structure of the metal site of Ni-SOD should play a key role both in fine-tuning the redox potential of the metal site and in the enzymatic mechanism.

Ni-SOD isolated from *Streptomyces seoulensis* was originally reported as a tetramer but now is known as a hexamer in its catalytically active form. Each subunit consists of 117 amino acids and one nickel ion with molecular mass of 13.4 kDa [18, 19]. Electron paramagnetic resonance (EPR) studies of the oxidized (resting) Ni-SOD showed that the active site contains Ni(III) ion with $g = [2.30\ 2.24\ 2.01]$ ($S = 1/2$) and that an axial position is occupied by a nitrogen ligand [16, 18–20]. X-ray crystallographic analyses of both the oxidized and the reduced Ni-SODs have shown that the nickel ion resides in the N-terminal loop. The active site of the reduced form

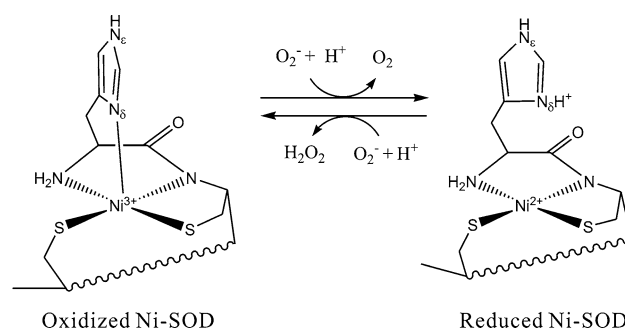


Fig. 1 Active-site structures of nickel-containing superoxide dismutase (Ni-SOD)

[Ni(II)] has a square-planar coordination with the amino group of His-1, the amide group of Cys-2, and two thiolate groups of Cys-2 and Cys-6 [18, 19]. The oxidized [Ni(III)] Ni-SOD has the axial ligand of the imidazole group of His-1 in addition to the equatorial ligands, forming a penta-coordinated square pyramid. The mechanistic conversion between the reduced and oxidized forms and the Ni(II)/Ni(III) redox potential are finely tuned by rotating the imidazole plane about the $C_\beta-C_\gamma$ bond of His-1 (Fig. 1). The mechanism of the dismutation by Ni-SOD is still controversial. X-ray structural analysis has suggested outer-sphere electron transfer [18], whereas EPR and X-ray crystallographic studies of Ni-SOD with inhibitor/inactivator have proposed inner-sphere electron transfer in which the superoxide ion is directly coordinated to the nickel ion in both oxidized and reduced forms at the side opposite His-1 imidazole [19].

Among the known redox-active nickel-containing enzymes, both carbon monoxide dehydrogenase and acetyl-coenzyme A synthase contain an active nickel center linked to an Fe–S cluster [21]. Methyl-coenzyme M reductase has a mononuclear nickel center, but there are no endogenous sulfur-donor ligands [22, 23]. [NiFe] hydrogenase also has a redox-active nickel center and is viewed as a Ni–Fe cluster bridged by two μ -thiolate sulfur atoms of cysteine residues [24]. Therefore, the active-site structure of Ni-SOD is a completely new class in redox-active nickel-containing enzymes, and the coordination and geometrical structure of the site and the related electronic structure are the keys to specifically controlling the dismutase activity of the enzyme. In the present study, we performed Q-band (35 GHz) $^{14}N, ^{1/2}H$ continuous wave (CW) and pulsed electron–nuclear double resonance (ENDOR) and ^{14}N X-band (9 GHz) electron spin echo envelope modulation (ESEEM) on the resting-state Ni(III)-SOD extracted from *S. seoulensis*. In-depth analyses of the data obtained from the multifrequency advanced-EPR techniques detail the electronic structure of the active site of Ni-SOD.

Materials and methods

Protein isolation

The Ni-SOD sample was prepared from *S. seoulensis* as described previously [15, 16], with some modifications. *S. seoulensis* was cultured in yeast extract/malt extract medium supplemented with 100 μM NiCl_2 to increase the expression of Ni-SOD. Mycelial cells of *S. seoulensis* harvested by aspiration on filter paper were resuspended in buffer A (20 mM phosphate buffer, pH 7.4). After cell disruption with an Omni-mixer (Omni International), cell debris was removed by centrifugation at 12,000g for 20 min. The supernatant was brought to a final 35% ammonium sulfate saturation and the precipitate was removed by centrifugation at 12,000g for 30 min. The resulting supernatant was loaded onto a phenyl-Sepharose CL-4B FastFlow column (5 cm \times 30 cm) equilibrated with buffer A containing ammonium sulfate at 35% saturation, and was eluted with a linear gradient of ammonium sulfate between 35 and 0% saturation. The fractions containing SOD activity were collected and desalted with a Sephadex G-25 column (8 cm \times 60 cm) equilibrated with buffer A. The desalted fractions were applied to a Protein-Pak DEAE 5PW column (2.15 cm \times 15 cm) using a Waters Delta Prep 4000 chromatography system and were separated using a linear gradient of 0.1–0.3 M NaCl. Active fractions were pooled and desalted using a YM10 membrane (Amicon), and were separated by preparative electrophoresis with a Bio-Rad model 491 prep cell apparatus using 7.5% nondenaturing polyacrylamide gel. After the active fractions had been concentrated using an Amicon YM10 membrane, the concentrated sample was loaded onto a Superdex 200 column (HiLoad 16/60) equilibrated with buffer A and was eluted with the same buffer by a fast protein liquid chromatography system (Pharmacia). The active fractions were further purified on a Mono Q column (HR 5/5) with a linear gradient of 0–0.3 M NaCl using the same fast protein liquid chromatography system. Finally, the purified Ni-SOD sample was mixed with an equal volume of ethylene glycol and loaded into the X-band or Q-band EPR quartz tube to be frozen at liquid-nitrogen temperature.

EPR/ENDOR/ESEEM measurements

X-band EPR spectra were collected at liquid-nitrogen temperature with a Bruker EMX spectrometer. Q-band CW EPR and ^1H , ^{14}N ENDOR spectra were collected using a modified Q-band Varian E-110 spectrometer equipped with a liquid-helium immersion Dewar at 2 K under rapid passage condition [25]. Q-band ^2H Mims ENDOR data were obtained with a locally built Q-band pulsed-EPR

spectrometer [26]. Three-pulse echo ($\pi/2-\tau-\pi/2-T-\pi/2-\tau$ -echo) intensities were recorded as a function of radio frequency to generate ^2H Mims ENDOR data [27].

The first-order ENDOR spectrum of a nucleus N with $I = 1/2$ in a paramagnetic center is a doublet with frequencies given by [28]

$$\nu_{\pm} = |\nu_{\text{N}} \pm A^{\text{N}}/2|. \quad (1)$$

Here, ν_{N} is the nuclear Larmor frequency and A^{N} is the angle-dependent hyperfine coupling constant. For a nucleus with $I \geq 1$, each ν_{\pm} transition is further split into $2I$ lines by the nuclear quadrupole interaction,

$$\nu_{\pm}(m_I) = |\nu_{\text{N}} \pm A^{\text{N}}/2 + (3P^{\text{N}}/2)(2m_I - 1)|, \quad (2)$$

where P^{N} is the angle-dependent quadrupole coupling constant and $-I + 1 \leq m_I \leq I$. For a frozen-solution sample with a rhombic EPR signal (g_1, g_2, g_3), the full hyperfine and quadrupole tensors, including both the principal values and the orientations in the \mathbf{g} -tensor axis frame, of the hyperfine-coupled nucleus can be obtained from the analysis of the 2D datasets comprising numerous ENDOR spectra collected across the EPR envelope, as described elsewhere [29–32].

X-band ^{14}N ESEEM experiments were performed on a locally built X-band pulsed-EPR spectrometer at 4 K [33]. Three-pulse echo ($\pi/2-\tau-\pi/2-T-\pi/2-\tau$ -echo) intensities were recorded as a function of the time interval T to construct the time-domain ESEEM data [34]. The $\pi/2$ microwave pulse duration was 16 ns with power of approximately 1 W. The frequency-domain spectra were obtained through Fourier transform of the time-domain data by modifying the “dead-time reconstruction” procedure originally developed by Mims [35].

Results

Q-band ^{14}N CW ENDOR

The resting-state Ni-SOD shows a well-resolved rhombic $S = 1/2$ EPR signal with $\mathbf{g} = [2.30 \ 2.24 \ 2.01]$ originating from a Ni(III) center. The g_3 (2.01) EPR signal is further split into three lines by 25 G (70 MHz) of the hyperfine coupling to an axial nitrogen ($I = 1$) ligand [16, 18–20]. Figure 2a shows the 20–45-MHz region of the Q-band CW ENDOR spectra obtained across the EPR envelope of the resting-state Ni-SOD. The “single-crystal-like” ENDOR spectrum obtained at the high-field edge (g_3) of the EPR spectrum shows two doublets centered at 35.2 MHz (circles in Fig. 2a) and each doublet splits by 3.0 MHz (“goal-post” marks in Fig. 2a). The centers of the two doublets are separated by 7.7 MHz, which is twice the ^{14}N Larmor frequency at the experimental magnetic field, indicating that

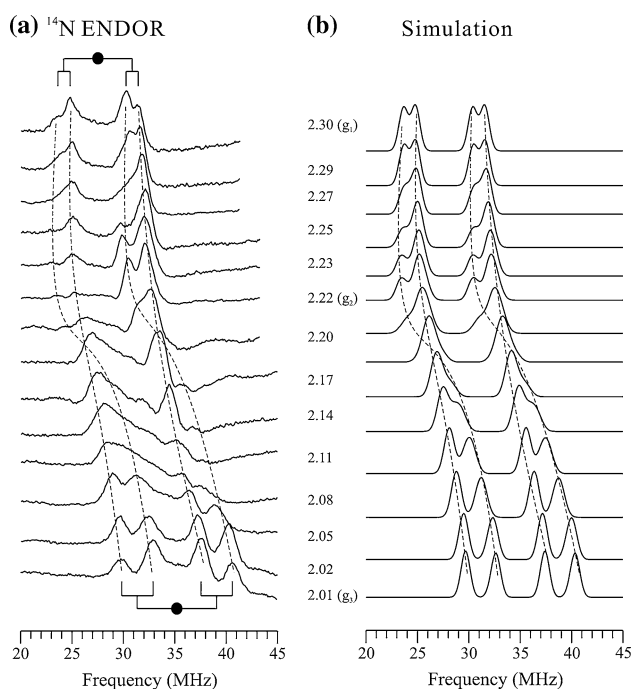


Fig. 2 **a** Q-band (35 GHz) ^{14}N continuous wave (CW) electron–nuclear double resonance (ENDOR) spectra of the resting-state (oxidized-state) Ni-SOD and **b** their corresponding numerical simulations. *Dashed lines* guide the change of the ENDOR pattern across the electron paramagnetic resonance (EPR) envelope. The experimental conditions were as follows: microwave frequency 35.252 GHz, modulation amplitude 1.3 G, radio-frequency (RF) power 20 W, RF sweep speed 1 MHz/s, and temperature 2 K. The simulation parameters were as follows: EPR linewidth 300 MHz and ENDOR linewidth 1 MHz. Other parameters were as in Table 1

the signal originates from a hyperfine-coupled ^{14}N nucleus; the observed ENDOR signal is hyperfine-centered [$35.2 \text{ MHz} = \mathbf{A}(g_3)/2$] and the separation within each doublet arises from the nuclear quadrupole coupling

[$3.0 \text{ MHz} = 3\mathbf{P}(g_3)$] (Eq. 2). Such a four-line pattern is also well observed at g_1 , the other “single-crystal-like” field position. The ^{14}N ENDOR signals are well followed across the EPR absorption envelope, although ENDOR line distortion is observed around g_2 because of slow nuclear relaxation, which is often the case in Q-band “rapid passage” ENDOR experiments. The observed field-dependent (orientation-selective) ^{14}N ENDOR data are well simulated, as shown in Fig. 2b, with the hyperfine coupling tensor $\mathbf{A} = [55 \ 55 \ 70.4] \text{ MHz}$ and the nuclear quadrupole coupling tensor $\mathbf{P} = [0.4 \ 0.6 \ -1.0] \text{ MHz}$, both of whose principal axes are coaxial to the \mathbf{g} -tensor frame [29–32] (Table 1).

X-band ^{14}N ESEEM

Figure 3a displays frequency-domain ^{14}N ESEEM spectra, obtained from Fourier transform of the time-domain ESEEM data, across the EPR of Ni-SOD. The numerical simulation of the data was obtained with the method developed previously [36]. Figure 3b depicts the results in a contour plot. The ^{14}N ESEEM collected at g_3 shows three well-resolved lines at about 0.55, about 1.05, and about 1.6 MHz, whose frequencies are almost invariant across the EPR envelope. Also one relatively broad band is observed at about 5.0 MHz in the ^{14}N ESEEM spectrum of g_3 . The position of this band shifts to lower frequencies as the g -value increases (or the magnetic field decreases).

This four-line pattern (three field-independent lines and one field-dependent band) of ^{14}N ESEEM is often observed when the nuclear Zeeman and half the nuclear hyperfine interactions are comparable. For this coupling condition, the nuclear Zeeman and hyperfine interactions are opposed and largely cancel in one electron-spin manifold, resulting in the nuclear states becoming nuclear quadrupole states [30]. All three nuclear transition lines from this manifold

Table 1 The nuclear hyperfine and quadrupole coupling tensors of the resting-state nickel-containing superoxide dismutase

Nucleus	Hyperfine coupling		Quadrupole coupling	
	Tensor (MHz) ^a	Orientation ^b	Tensor (MHz) ^a	Orientation ^b
$^{14}\text{N}_\delta^c$	[55 55 70.4] ^d	(0° 0° 0°)	[0.4 0.6 -1.0] ^d	(0° 0° 0°)
$^{14}\text{N}_e^e$	[1.9 2.0 2.7] ^d	(90° 10° 90°)	[0.18 0.65 -0.83] ^f	(0° 65° 0°)
$^1\text{H}^g$	[-3.8 -3.8 10.6] ^h	(30° 70° 0°)	–	–

^a The signs are arbitrary

^b Euler angles with respect to \mathbf{g} -tensor frame [46, 47]. The error range is $\pm 5^\circ$

^c Axial ligand

^d The error range is $\pm 0.5 \text{ MHz}$

^e Remote nitrogen

^f $e^2qQ = 1.65 \text{ MHz} (\pm 0.05)$, $\eta = 0.57 (\pm 0.03)$

^g Solvent-exchangeable strongly coupled proton

^h $r_{\text{eff}}(\text{Ni-H}) = 2.55 \text{ \AA} (\pm 0.05)$, $A_{\text{iso}} = 1.0 \text{ MHz} (\pm 0.05)$

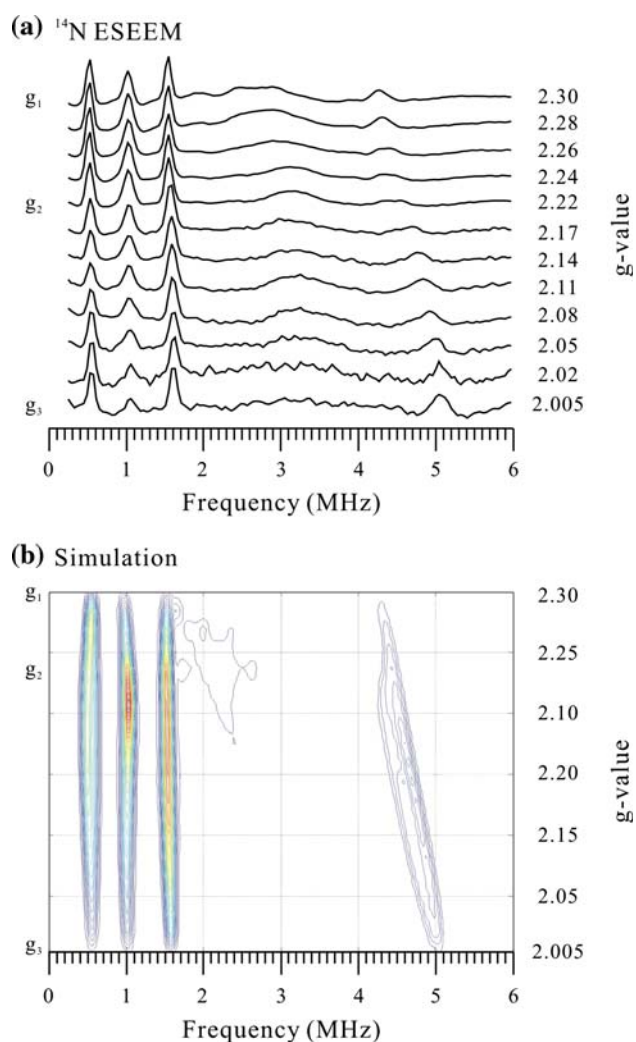


Fig. 3 **a** X-band (9 GHz) ^{14}N three-pulse electron spin echo envelope modulation (ESEEM) frequency-domain (Fourier transform) spectra of the resting-state (oxidized-state) Ni-SOD and **b** their corresponding numerical simulations in a 2D contour plot. The experimental conditions were as follows: microwave frequency 9.714 GHz, $\tau \sim 140$ ns, shot repetition time 24 ms, and temperature 4 K. For the simulation, the ^{14}N nuclear hyperfine and quadrupole tensors were as in Table 1

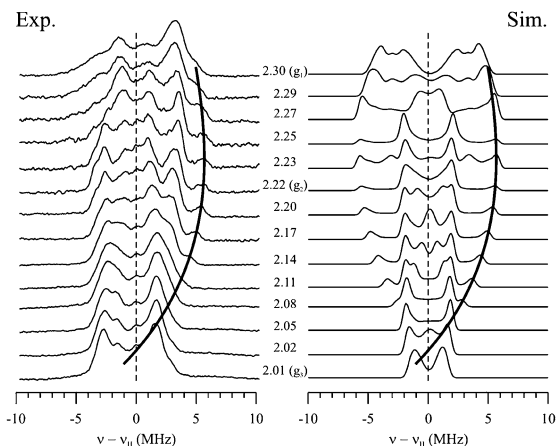
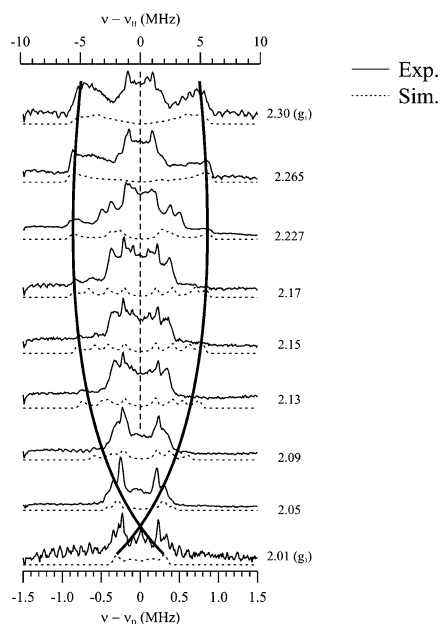
are primarily determined by the nuclear quadrupole coupling constant, which is independent of the external magnetic field. Therefore, the lines are usually narrow and the frequencies are mostly independent of the field strength. In the other electron spin manifold, the nuclear Zeeman and hyperfine interactions are additive. Single-quantum transitions ($\Delta m_I = \pm 1$) in this manifold depend on the orientation of the magnetic field and give rise to a broad powder-ESEEM spectrum, seldom observed in time-domain experiment. However, the double-quantum transition ($\Delta m_I = \pm 2$) is weakly dependent on the orientation of the magnetic field and thus is readily detected. The double-quantum transition frequency varies according to the

strength of the magnetic field because it is dependent on the nuclear Zeeman interaction as well as the nuclear hyperfine and quadrupole tensors [36].

Numerical simulation (Fig. 3b), based on the frequency-domain orientation-selective ^{14}N ESEEM analysis method [36], shows that the observed ^{14}N nucleus has a nuclear hyperfine coupling tensor of $\mathbf{A} = [1.9 \ 2.0 \ 2.7]$ MHz and a nuclear quadrupole coupling constant of $e^2qQ = 1.65$ MHz with an asymmetry parameter of $\eta = 0.57$. The simulation found that the lineshape and the field-dependent frequency position of the double-quantum transition band were sensitive to the relative orientation of the hyperfine tensor with respect to the \mathbf{g} -tensor frame, whereas those of the three narrow transition lines of the nuclear quadrupole states were sensitive to the relative orientation of the quadrupole tensor, yielding Euler angles of $[\alpha \ \beta \ \gamma] = [90^\circ \ 10^\circ \ 90^\circ]$ for the hyperfine tensor and $[\alpha \ \beta \ \gamma] = [0^\circ \ 65^\circ \ 0^\circ]$ for the quadrupole tensor with respect to the \mathbf{g} -tensor frame. An unresolved ^{14}N ESEEM feature found in the 2–4-MHz region (Fig. 3a) may come from weakly coupled ^{14}N or the $\Delta m_I = \pm 1$ transition.

Q-band ^1H ENDOR

The left panel in Fig. 4a shows the Q-band ^1H CW ENDOR spectra obtained across the EPR envelope of the resting-state Ni(III)-SOD. The ENDOR spectrum collected at the low-field edge (g_1) exhibits at least three doublets, centered at the ^1H Larmor frequency, arising from the protons hyperfine-coupled to the Ni(III) center. The field-dependent patterns of the signals are not completely resolved owing to overlaps of the powder-ENDOR lineshapes. However, the outermost ν_+ pattern of the strongly coupled (10.2 MHz at g_1) ^1H signals are easily followed (dark lines in Fig. 4a). These strongly coupled signals were absent in the ^1H ENDOR spectra of Ni-SOD incubated in D_2O buffer, indicating the signals arise from a solvent-exchangeable proton. As seen in the right panel in Fig. 4a, the ENDOR pattern of the exchangeable proton is well simulated by a through-space point-dipole approximation with an effective distance of $r_{\text{eff}}(\text{Ni(III)}-^1\text{H}) = 2.55$ Å and an isotropic coupling of $A_{\text{iso}}(^1\text{H}) = 1.0$ MHz. The Ni(III) \rightarrow ^1H vector is estimated as lying at $\theta = 70^\circ$ and $\phi = 30^\circ$ with respect to the \mathbf{g} -tensor frame. The ^2H nucleus corresponding to the exchangeable proton can be detected by ^2H Mims ENDOR of Ni-SOD incubated in D_2O buffer. Figure 4b shows such data (solid lines) along with the simulation (dotted lines) using the corresponding ^2H hyperfine coupling constant ($|A(^1\text{H})/A(^2\text{H})| = 6.51$) and the orientation vector, confirming that the strongly coupled proton observed by ^1H CW ENDOR is solvent-exchangeable. ^2H Mims ENDOR also reveals other solvent-exchangeable protons with $|A(^2\text{H})| \leq 0.75$ MHz, corresponding to $|A(^1\text{H})| \leq 5.0$ MHz ($r_{\text{eff}}(\text{Ni}-\text{H}) \geq 3.2$ Å).

(a) ^1H CW ENDOR(b) ^2H Mims ENDOR

Discussion

The EPR spectrum of the resting-state Ni-SOD shows a well-resolved rhombic $S = 1/2$ EPR signal with $\mathbf{g} = [2.30 \ 2.24 \ 2.01]$. The \mathbf{g} -tensor feature is well characterized as a Ni(III) center with a d_{z^2} ground state in a tetragonally distorted octahedral or square-pyramidal geometry. A slight contribution of $d_{x^2-y^2}$ to the ground state causes g_3 (2.01) to be slightly larger than 2.00. The rhombicity of the \mathbf{g} tensor indicates that the d_{xz} and d_{yz} orbitals are not degenerate. The g_3 (2.01) EPR signal is further split into three lines by 25 G (70 MHz) of the hyperfine coupling to an axial nitrogen ($I = 1$) ligand. The axial nitrogen has been identified as N_δ of His-1 imidazole of Ni-SOD by X-ray crystallographic studies of the oxidized enzyme

◀ **Fig. 4** a Q-band (35 GHz) ^1H CW ENDOR spectra of the resting-state (oxidized-state) Ni-SOD (*left*) and their corresponding numerical simulations for the solvent-exchangeable strongly coupled proton (*right*). The spectra are centered at the proton Larmor frequencies. *Dark lines* denote the outermost pattern of the ν_+ line of the solvent-exchangeable strongly coupled ^1H signals. The experimental conditions were as follows: microwave frequency 35.255 GHz, modulation amplitude 1.3 G, RF power 20 W, RF sweep speed 1 MHz/s, and temperature 2 K. The simulation parameters were as follows: EPR linewidth 200 MHz and ENDOR linewidth 0.5 MHz. The other parameters were as in Table 1. **b** Q-band (35 GHz) ^2H Mims ENDOR spectra of the resting-state (oxidized-state) Ni-SOD in D_2O buffer (*solid lines*) and their corresponding numerical simulations for the strongly coupled ^2H (*dashed lines*). The spectra are centered at the deuterium Larmor frequencies. Corresponding proton frequencies centered at the proton Larmor frequencies are marked at the *top*. *Dark lines* denote the outermost patterns of the ν_+ and ν_- lines of the solvent-exchangeable strongly coupled ^2H signals. The experimental conditions were as follows: microwave frequency 34.858 GHz, $\tau = 332$ ns, microwave pulse width 52 ns, RF pulse width 30 μs , shot repetition time 10 ms, and temperature 2 K. The simulation parameters were as follows: EPR linewidth 200 MHz, ENDOR linewidth 0.05 MHz, the ^2H hyperfine coupling tensor values were 1/6.51th of the ^1H hyperfine coupling tensor values and the orientation was the same, and the nuclear quadrupole tensor $\mathbf{P} = [0.07 \ 0.07 \ -0.14]$ MHz with Euler angles of $(90^\circ \ 35^\circ \ 0^\circ)$

[18, 19]. Further, the structural study revealed that the equatorial plane of the Ni(III) site is occupied by the amino group of His-1, the amide group of Cys-2, and two thiolate groups of Cys-2 and Cys-6, to form a square-pyramidal coordination geometry with the axial nitrogen.

Analysis of Q-band ^{14}N CW ENDOR data (Fig. 2) yields the hyperfine coupling tensor, $\mathbf{A} = [55 \ 55 \ 70.4]$ MHz, and the nuclear quadrupole coupling tensor, $\mathbf{P} = [-0.4 \ -0.6 \ 1.0]$ MHz, of the axial nitrogen (Table 1). The large isotropic hyperfine coupling ($A_{\text{iso}} = 60$ MHz) is comparable to those of axial nitrogen ligands of Ni(III) complexes with square-pyramidal geometry [37–41] and results from spin delocalization through the σ -bond between the metal d_{z^2} and the axial nitrogen (N_δ), as is common for Ni(III)–imidazole complexes.

For metal–nitrogen complexes, the ^{14}N nuclear quadrupole coupling is sensitive to details of the metal–nitrogen bond. The largest ^{14}N nuclear quadrupole coupling can be either along the metal–nitrogen bond (nitrogen lone pair direction) or normal to the metal–nitrogen bond. The former shows a negative coupling constant, whereas the latter, occurring with increasing nitrogen-to-metal donation as found in copper(II) tetraphenylporphyrin and aquometmyoglobin, shows a positive coupling constant [42]. In Ni-SOD, the ^{14}N nuclear quadrupole and nuclear hyperfine coupling tensors of the axial nitrogen are collinear with the \mathbf{g} tensor (Table 1) and the largest ^{14}N nuclear quadrupole coupling (P_3) is along the Ni(III)– N_δ bond. For the tetragonally distorted (or square-pyramidal) $S = 1/2$ Ni(III), the orientations of the d_{yz} and d_{xz} orbitals affect the directions of the g_1 (equivalent to g_x) and g_2 (equivalent to g_y)

components of the **g** tensor, respectively. The collinearity of the **g** and ^{14}N nuclear quadrupole tensors can be explained by metal-to-nitrogen π back-donation. A favorable orientation of either the filled d_{yz} or the filled d_{xz} orbital for back-donation to the empty nitrogen p_π orbital [43], normal to the imidazole plane, strengthens the metal–nitrogen bond and causes the coincidence of the **g** and **P** tensors. In other words, for the tetragonally distorted (or square-pyramidal) $S = 1/2$ Ni(III) complexes with axial imidazole, the **g**-tensor direction is modulated by the imidazole plane.

X-band ^{14}N ESEEM measurements (Fig. 3) identified one well-defined signal from a ^{14}N atom with the hyperfine tensor **A** = [1.9 2.0 2.7] MHz, plus the possibility of other weakly coupled nitrogen(s). There are four nitrogen atoms present within the magnetic-coupling range of the Ni(III) center of Ni-SOD; the imidazole N_δ and N_ϵ of His-1, the terminal amine nitrogen of His-1, and the amide nitrogen of Cys-2. The strongly coupled imidazole N_δ of His-1 was characterized by Q-band ^{14}N CW ENDOR (Fig. 1). For spin-bearing metal-bound imidazole, the hyperfine coupling of the nitrogen directly bound to the metal is in general 20–30 times bigger than that of the remote nitrogen. This enables us to assign the well-defined nitrogen signal seen by ESEEM to the imidazole N_ϵ of His-1 (remote nitrogen). In-plane coordinated ^{14}N atoms have minimal coupling to an electron in the d_{z^2} orbital.

The crystallographic studies of the reduced Ni-SOD have shown that the imidazole of His-1 donates two hydrogen bonds, $\text{N}_\delta\text{-H}\cdots\text{O}_{\text{Val-8}}$ and $\text{N}_\epsilon\text{-H}\cdots\text{O}_{\text{Glu-17}}$. Upon oxidation of the enzyme, the hydrogen bond of $\text{N}_\epsilon\text{-H}\cdots\text{O}_{\text{Glu-17}}$ remains, whereas that of $\text{N}_\delta\text{-H}\cdots\text{O}_{\text{Val-8}}$ is broken and N_δ is bound to Ni(III) [18, 19]. The ^{14}N nuclear quadrupole coupling parameters of the remote nitrogen of a metal-bound imidazole have been widely utilized to study the chemical environment, which tunes the electron density of the remote nitrogen. The ^{14}N nuclear quadrupole coupling constant $e^2qQ = 1.67$ MHz and the asymmetry parameter $\eta = 0.57$ of the remote nitrogen (N_ϵ) of His-1 of Ni-SOD are close to the values expected when there is a weak or no hydrogen bonding to the remote N–H [44, 45]. This suggests that there is a subtle change in the hydrogen-bonding network around the active sites in crystal and solution phases in the Ni(III) state.

Q-band ^1H CW ENDOR and pulsed ^2H Mims ENDOR show that the hyperfine couplings (10.2 MHz at g_1) to the strongly coupled solvent-exchangeable proton(s) are mostly dipolar (Fig. 4). From the point-dipole approximation, assuming 100% spin on Ni(III), the effective distance (r_{eff}) between Ni(III) and the proton is estimated to be approximately 2.55 Å (Table 1). The Ni(III) \rightarrow H vector with $\theta = 70^\circ$ and $\phi = 30^\circ$ in the **g**-tensor frame indicates that the coupled proton(s) is near the g_1 – g_2 plane (equatorial ligand plane). The crystal structure shows the

distance from Ni(III) to the amine nitrogen of His-1 is 2.182 Å. Assuming the bond length of the amine N–H is about 1 Å and the Ni(III)–N–H angle adopts near tetrahedral geometry, we estimate the Ni(III)– H_{amine} distance to be approximately 2.3 Å. This enables us to assign the proton giving rise to the hyperfine coupling to the proton(s) of the terminal amine nitrogen of His-1. The difference between ENDOR and crystallographic distances reflects the delocalization of the spin density.

Q-band $^{1/2}\text{H}$ ENDOR also found weakly coupled solvent-exchangeable proton(s), for which the effective distance is no less than 3.2 Å ($|\text{A}(\text{H})| \leq 5.0$ MHz). In the framework of the protein backbone, solvent-exchangeable protons are not present within the detected hyperfine-coupling range. The crystal structure shows a vacant pocket, enclosed by the backbone and side chains of Cys-2 through Cys-6, on the side opposite the axial N_δ . This pocket embeds a water molecule at a distance of 3.427 Å from Ni(III) in the crystal. The weakly coupled solvent-exchangeable proton thus seems to be the proton(s) of this water. But, as a kind reviewer pointed, the possibility of the proton of a water molecule being hydrogen-bonded to the equatorial thiolate ligand cannot be ruled out.

In summary, we performed ENDOR and ESEEM experiments to obtain details on the electronic structure and magnetic couplings of the Ni(III) site of Ni-SOD. The analysis of the field-dependent Q-band ^{14}N CW ENDOR determined the nuclear hyperfine and quadrupole coupling tensors of the axial ^{14}N ligand of Ni(III), N_δ of His-1 imidazole. The tensors are coaxial with the **g**-tensor frame, implying the **g**-tensor direction is modulated by the imidazole plane. X-band ^{14}N ESEEM characterizes the weakly coupled N_ϵ of His-1 imidazole. The nuclear quadrupole coupling constant of this nitrogen suggests that the hydrogen-bonding between $\text{N}_\epsilon\text{-H}$ and $\text{O}_{\text{Glu-17}}$ present for the reduced-state Ni-SOD is weakened or broken in the Ni(III) enzyme in aqueous phase. Q-band ^1H CW ENDOR and pulsed ^2H Mims ENDOR distinguished two kinds of solvent-exchangeable protons: one is the equatorial amine proton(s) of His-1 and the other is either the proton(s) of a water in the pocket at the side opposite the axial N_δ or the proton of a water hydrogen-bonded to the equatorial thiolate ligand.

Acknowledgments This work was supported by the Korea Research Foundation (KRF-2006-312-C00219, H.I.L.), the Research Fellowship of BK21 project (S.O.K.), and the NSF (MCB0723330, B.M.H.).

References

1. Fridovich I (1997) *J Biol Chem* 272:18515–18517
2. Cabelli DE, Riley D, Rodriguez JA, Valentine JS, Zhu H (2000). In: Meunier B (ed) *Biomimetic oxidations catalyzed by transition metal complexes*. Imperial College Press, London, chap 10

3. Miller A-F (2003) In: Que L Jr, Tolman W (eds) *Coordination chemistry in the biosphere and geosphere*. Pergamon, Amsterdam, pp 479–506
4. Miller A-F (2004) *Curr Opin Chem Biol* 8:162–168
5. Tainer JA, Getzoff ED, Richardson JS, Richardson DC (1983) *Nature* 306:284–287
6. Bordo D, Djinovic-Carugo K, Bolognesi M (1994) *J Mol Biol* 238:366–368
7. Djinovic-Carugo K, Battistoni A, Carri M, Polticelli F, Desideri A, Rotilio G, Coda A, Wilson K, Bolognesi M (1996) *Acta Crystallogr D* 52:176–188
8. Bordo D, Matak D, Djinovic-Carugo K, Rosano C, Pesce A, Bolognesi M, Stoppolo ME, Falconi M, Battistoni A, Desideri A (1999) *J Mol Biol* 285:283–296
9. Parker MW, Blake CC (1988) *J Mol Biol* 199:649–661
10. Ludwig ML, Metzger AL, Patridge KA, Stallings WC (1991) *J Mol Biol* 219:335–358
11. Borgstahl GE, Parge HE, Hickey MJ, Beyer WF Jr, Hallewell RA, Tainer JA (1992) *Cell* 71:107–118
12. Edwards RA, Whittaker MM, Whittaker JW, Jameson GB, Baker EN (1998) *J Am Chem Soc* 120:9684–9685
13. Lah MS, Dixon MM, Patridge KA, Stallings WC, Fee JA, Ludwig ML (1995) *Biochemistry* 34:1646–1660
14. Guan Y, Hickey MJ, Borgstahl GEO, Hallewell RA, Lepock JR, O'Connor D, Hsieh Y, Nick HS, Silverman DN, Tainer JA (1998) *Biochemistry* 37:4722–4730
15. Youn H-D, Kim E-J, Roe J-H, Hah YC, Kang S-O (1996) *Biochem J* 318:889–896
16. Youn H-D, Youn H, Lee J-W, Yim Y-I, Lee J-K, Hah YC, Kang S-O (1996) *Arch Biochem Biophys* 334:341–348
17. Dupont CL, Neupane K, Shearer J, Palenik B (2008) *Environ Microbiol* 10:1831–1843
18. Wuerges J, Lee J-W, Yim Y-I, Yim H-S, Kang S-O, Djinovic-Carugo K (2004) *Proc Natl Acad Sci USA* 101:8569–8574
19. Barondeau DP, Kassmann CJ, Bruns CK, Tainer JA, Getzoff ED (2004) *Biochemistry* 43:8038–8047
20. Choudhury SB, Lee J-W, Davidson G, Yim Y-I, Bose K, Sharma ML, Kang S-O, Cabelli DE, Maroney MJ (1999) *Biochemistry* 38:3744–3752
21. Evans DJ (2005) *Coord Chem Rev* 249:1582–1595
22. Kraulis PJ (1991) *J Appl Crystallogr* 24:946–950
23. Merritt EA, Murphy MEP (1994) *Acta Crystallogr D* 50:869–873
24. Fontecilla-Camps JC, Volbeda A, Cavazza C, Nicolet Y (2007) *Chem Rev* 107:4273–4303
25. Werst MM, Davoust CE, Hoffman BM (1991) *J Am Chem Soc* 113:1533–1538
26. Davoust CE, Doan PE, Hoffman BM (1996) *J Magn Reson* 119:38–44
27. Schweiger A, Jeschke G (2001) *Principles of pulse electron paramagnetic resonance*. Oxford University Press, Oxford
28. Abragam A, Bleaney B (1986) *Electron paramagnetic resonance of transition ions*. Dover, New York
29. Hoffman BM, Martinsen J, Venters RA (1984) *J Magn Reson* 59:110–123
30. Hoffman BM, Venters RA, Martinsen J (1985) *J Magn Reson* 62:537–542
31. Hoffman BM, DeRose VJ, Doan PE, Gurbiel RJ, Houseman ALP, Telser J (1993) *Biol Magn Reson* 13:151–218
32. Doan PE (2003) In: Telser J (ed) *Paramagnetic resonance of metallobiomolecules*. American Chemical Society, Washington, pp 55–81
33. Fan CL, Doan PE, Davoust CE, Hoffman BM (1992) *J Magn Reson* 98:62–72
34. Dikanov SA, Tsvetkov YD (1992) *Electron spin echo envelope modulation (ESEEM) spectroscopy*. CRC, Boca Raton
35. Mims WB (1984) *J Magn Reson* 59:291–306
36. Lee H-I, Doan PE, Hoffman BM (1999) *J Magn Reson* 140:91–107
37. Lappin AG, Murray CK, Margerum DW (1978) *Inorg Chem* 17:1630–1634
38. Lovecchio FV, Gore ES, Busch DH (1974) *J Am Chem Soc* 96:3109–3118
39. Pinho D, Gomes P, Freire C, de Castro B (2001) *Eur J Inorg Chem* 2001(6):1483–1493
40. Wang YL, Beach MW, Pappenhagen TL, Margerum DW (1988) *Inorg Chem* 27:4464–4472
41. Seth J, Palaniappan V, Bocian DF (1995) *Inorg Chem* 34:2201–2206
42. Brown TG, Hoffman BM (1980) *Mol Phys* 39:1073–1109
43. Telser J, Fann Y-C, Renner MW, Fajer J, Wang S, Zhang H, Scott RA, Hoffman BM (1997) *J Am Chem Soc* 119:733–743
44. Jiang F, McCracken J, Peisach J (1990) *J Am Chem Soc* 112:9035–9044
45. Colaneri MJ, Peisach J (1992) *J Am Chem Soc* 114:5335–5341
46. Mathews J, Walker RL (1965) *Mathematical methods of physics*. Benjamin, Elmsford
47. True E, Nelson MJ, Venters RA, Orme-Johnson WH, Hoffman BM (1988) *J Am Chem Soc* 110:1935–1943